ELSEVIER

Volume 184, Issue 2, February 2011

CONTENTS

JOURNAL OF SOLID STATE CHEMISTRY

www.elsevier.com/locate/jssc

Abstracted/indexed in BioEngineering Abstracts, Chemical Abstracts, Coal Abstracts, Current Contents/Physics, Chemical, & Earth Sciences, Engineering Index, Research Alert, SCISEARCH, Science Abstracts, and Science Citation Index. Also covered in the abstract and citation database SCOPUS®. Full text available on ScienceDirect®.

Regular Articles

Magnetic and transport properties of $RCr_{0.3}Ge_2$ (R = Tb, Dy, Ho and Er) compounds
A. Gil, D. Kaczorowski, B. Penc, A. Hoser and A. Szytuła
page 227

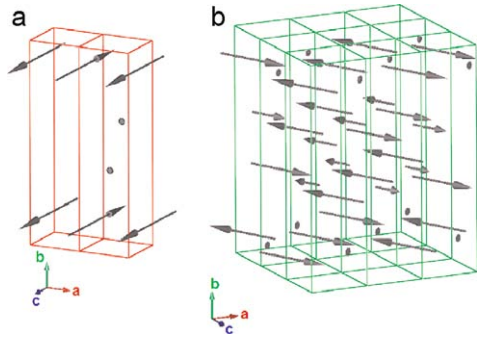

In the neutron diffraction pattern of $TbCr_{0.3}Ge_2$ compound collected at 1.5 K the additional peaks of magnetic origin form two groups. The first one, with strong intensities, can be indexed by the propagation vector $\mathbf{k}=(12,0,0)$ (a), while the second one, with small intensities, can be described by the propagation vector $\mathbf{k}=(14,0,14)$ (b). The analysis of the magnetic peak intensities indicates that the Tb magnetic moments located at the positions Tb1 $(0,y,14)$, Tb2 $(0,-y,34)$, Tb3 $(12,12+y,14)$ and Tb4 $(12,12-y,34)$ form a collinear structure with the $(+\ +\ -\ -)$ sequence in the crystallographic unit cell for the first component and $(-\ +\ +\ -)$ for the second.

Distribution-related luminescence of Eu^{3+} sensitized by SnO_2 nano-crystals embedding in oxide glassy matrix
Yunlong Yu, Daqin Chen, Ping Huang, Hang Lin, Anping Yang and Yuansheng Wang
page 236

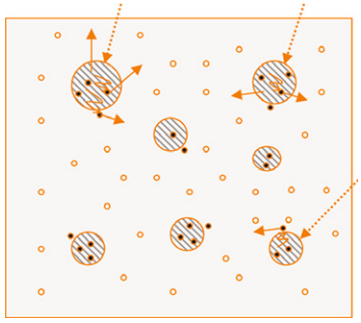

The Eu^{3+} distribution-related energy transfer behavior in transparent glass ceramics embedding SnO_2 nano-crystals.

Regular Articles—Continued

Heat capacity, enthalpy and entropy of ternary bismuth tantalum oxides
J. Leitner, V. Jakeš, Z. Sofer, D. Sedmidubský, K. Růžička and P. Svoboda
page 241

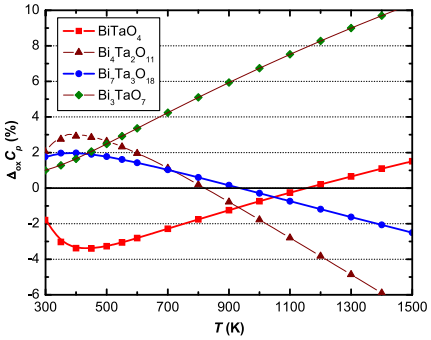

Temperature dependence of $\Delta_{ox}C_{pm}$ for bismuth tantalum mixed oxides.

Polyol-mediated solvothermal synthesis and luminescence properties of CeF_3, and CeF_3:Tb^{3+} nanocrystals
Xuesong Qu, Hyun Kyoung Yang, Jong Won Chung, Byung Kee Moon, Byung Chun Choi, Jung Hyun Jeong and Kwang Ho Kim
page 246

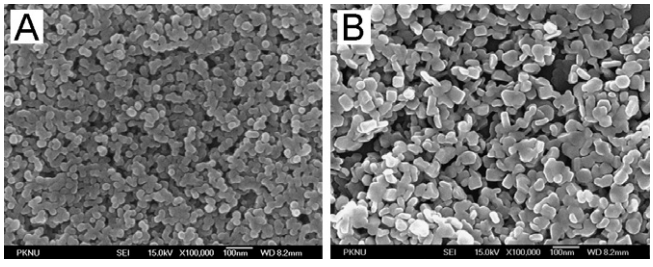

0D nanoparticles and 2D nanoplates CeF_3 and CeF_3:Tb^{3+} have been successfully fabricated through a facile polyol process.

Continued

Synthesis, structure and characterisation of the $n=4$ Aurivillius phase $Bi_5Ti_3CrO_{15}$
A.T. Giddings, M.C. Stennett, D.P. Reid, E.E. McCabe, C. Greaves and N.C. Hyatt
page 252

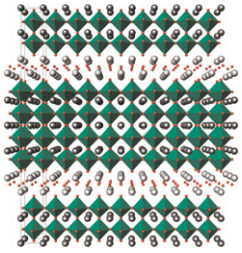

We report here the synthesis, structure and characterisation of the $n=4$ Aurivillius phase $Bi_5Ti_3CrO_{15}$. Analysis of neutron powder diffraction and XANES data, supported by Madelung energy calculations, demonstrate partial ordering of Ti and Cr cations in the component perovskite layer. $Bi_5Ti_3CrO_{15}$ is paramagnetic in the temperature range studied but exhibits a dielectric and DSC anomaly at 660 °C, characteristic of a ferroelectric–paraelectric phase transition. Analysis of high temperature neutron diffraction data confirm a direct phase transition between space groups $A2_1am$ and $I4/mmm$ at ~660 °C.

Preparation, characterization, magnetic susceptibility (Eu, Gd and Sm) and XPS studies of Ln_2ZrTiO_7 (Ln = La, Eu, Dy and Gd)
B. Vijaya Kumar, Radha Velchuri, V. Rama Devi, B. Sreedhar, G. Prasad, D. Jaya Prakash, M. Kanagaraj, S. Arumugam and M. Vithal
page 264

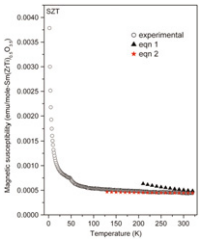

Sm_2ZrTiO_7 does not follow the Curie or the Curie–Weiss law. The effective magnetic moment is found to be 0.768 BM (at 300 K), which is smaller than the free ion moment 1.3–1.4 BM.

Improved conversion efficiency in dye-sensitized solar cells based on electrospun Al-doped ZnO nanofiber electrodes prepared by seed layer treatment
Sining Yun and Sangwoo Lim
page 273

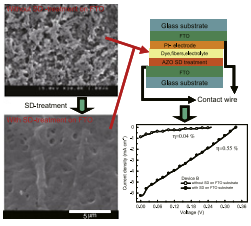

The poor adhesion between electrospun nanofibers and substrate is improved by a simple and facile seed layer (SD) treatment. The energy conversion efficiency of AZO nanofiber-based DSSCs has been greatly increased by SD-treatment of the FTO substrate.

A series of Cd(II) complexes with π–π stacking and hydrogen bonding interactions: Structural diversities by varying the ligands
Xiuli Wang, Jinxia Zhang, Guocheng Liu and Hongyan Lin
page 280

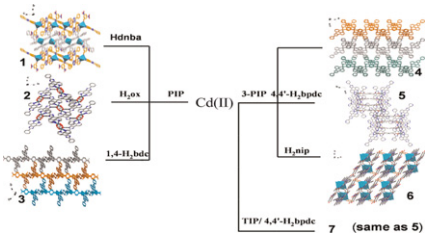

Seven new supramolecular architectures have been successfully isolated under hydrothermal conditions by reactions of different phen derivatives and Cd(II) salts together with organic carboxylate anions auxiliary ligands.

The effect of the distance between acidic site and basic site immobilized on mesoporous solid on the activity in catalyzing aldol condensation
Xiaofang Yu, Xiaobo Yu, Shujie Wu, Bo Liu, Heng Liu, Jingqi Guan and Qiubin Kan
page 289

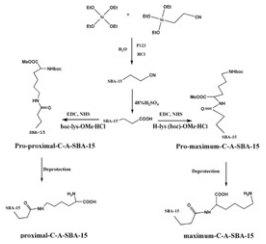

Proximal-C-A-SBA-15 with a proximal acid–base distance and maximum-C-A-SBA-15 with a maximum acid–base distance were synthesized by immobilizing lysine onto carboxyl-SBA-15.

High-pressure high-temperature synthesis and crystal structure of the isotypic rare earth (RE)–thioborate–sulfides $RE_9[BS_3]_2[BS_4]_3S_3$, (RE = Dy–Lu)
Marija Borna, Jens Hunger, Alim Ormeci, Dirk Zahn, Ulrich Burkhardt, Wilder Carrillo-Cabrera, Raul Cardoso-Gil and Rüdiger Kniep
page 296

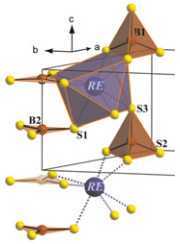

Isotypic rare earth–thioborate–sulfides $RE_9[BS_3]_2[BS_4]_3S_3$, (RE = Dy–Lu) were prepared by application of high-pressure high-temperature conditions to mixtures of the elements. Their crystal structures are characterized by presence of the two isolated complex ions $[BS_3]^{3-}$ and $[BS_4]^{5-}$ as well as $[\square(S^{2-})_3]$ units. Quantum mechanical calculations revealed the arrangement of the intrinsic vacancies.

CO_2 capture properties of *M*–C–O–H (*M* = Li, Na, K) systems: A combined density functional theory and lattice phonon dynamics study
Yuhua Duan, Bo Zhang, Dan C. Sorescu and J. Karl Johnson
page 304

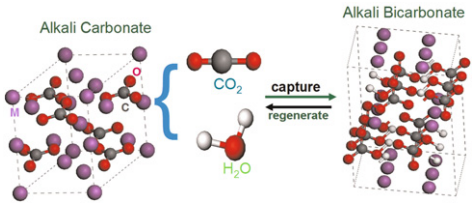

The calculated results indicate that the $Na_2CO_3/NaHCO_3$ and $K_2CO_3/KHCO_3$ systems are the most promising candidates of all those we investigated for both pre-and post-combustion CO_2 capture.

Synthesis of Au/SnO_2 core–shell structure nanoparticles by a microwave-assisted method and their optical properties
Yeon-Tae Yu and Prabir Dutta
page 312

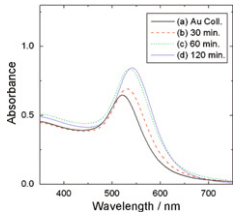

In microwave preparation, the peak position of UV–visible absorption band of Au nanoparticles was red-shifted from 520 to 543 nm, due to the formation of an SnO_2 shell with high crystallinity.

The effect of refluxing on the alkoxide-based sodium potassium niobate sol–gel system: Thermal and spectroscopic studies
Anirban Chowdhury, Jonathan Bould, Michael G.S. Londesborough and Steven J. Milne
page 317

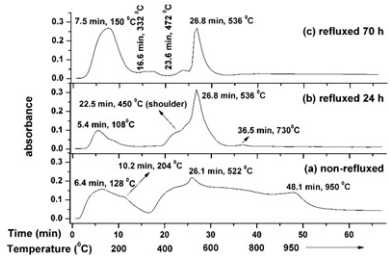

Total organic evolution plots over time for NKN dried gels obtained under different refluxing times show different thermo-chemical behaviours and these were investigated by thermal and spectroscopic analysis tools to find a correlation between the extent of –M–O–M– chain link formation and the amount of solvent vapour (methoxyethanol) evolution.

The new ternary silicide Gd_5CoSi_2: Structural, magnetic and magnetocaloric properties
Charlotte Mayer, Etienne Gaudin, Stéphane Gorsse and Bernard Chevalier
page 325

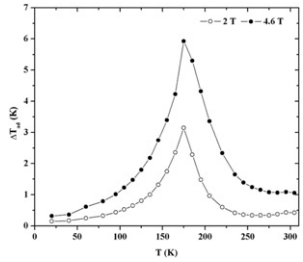

The adiabatic temperature change ΔT_{ad} was determined by combining the heat capacity measurements and the magnetization data. As expected, a peak near the Curie temperature of the Gd_5CoSi_2 ternary silicide is observed, with a maximum of ΔT_{ad} around 3.1 and 5.9 K for $\Delta H = 2$ and 4.6 T, respectively.

Novel alkylimidazolium/vanadium pentoxide intercalation compounds with excellent adsorption performance for methylene blue
AiGuo Kong, Yong Jie Ding, Ping Wang, Heng Qiang Zhang, Fan Yang and Yong Kui Shan
page 331

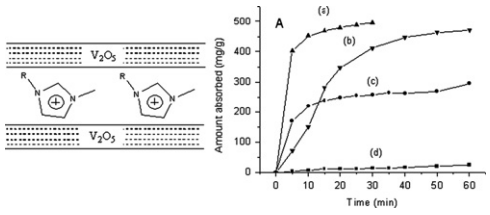

The alkylimidazolium-intercalated V_2O_5 compounds with special straw-like nanofiber morphology were synthesized by a redox reaction between iodide ion and V_2O_5, which show the excellent adsorption performance for methylene blue in an aqueous medium.

Syntheses and single-crystal structures of $CsTh(MoO_4)_2Cl$ and $Na_4Th(WO_4)_4$
Geng Bang Jin and L. Soderholm
page 337

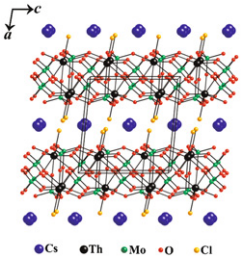

The two-dimensional layered structure of $CsTh(MoO_4)_2Cl$ viewed down the *b* axis.

Continued

Structural, thermodynamic and optical properties of MgF_2 studied from first-principles theory
K. Ramesh Babu, Ch. Bheema Lingam, S. Auluck, Surya P. Tewari and G. Vaitheeswaran
page 343

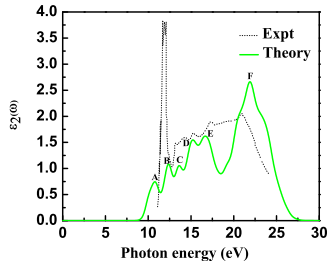

The calculated imaginary part ε2(ω) of the complex dielectric function ε(ω) of MgF_2 as a function of photon energy is shown. The calculated ε2(ω) could reproduce the major peaks observed in experiment. All the peaks observed are corresponds to interband transitions from '*p*' states of Fluorine in valence band to the '*s*' states of Mg in conduction band.

Unexpected formation by pulsed laser deposition of nanostructured Fe/olivine thin films on MgO substrates
C. Legrand, L. Dupont, C. Davoisne, F. Le Marrec, J. Perrière and E. Baudrin
page 351

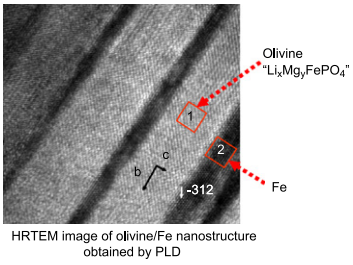

HRTEM image of olivine/Fe nanostructure obtained by PLD

HRTEM image of olivine/Fe nanostructure obtained by PLD.

$CdWO_4$ polymorphs: Selective preparation, electronic structures, and photocatalytic activities
Tingjiang Yan, Liping Li, Wenming Tong, Jing Zheng, Yunjian Wang and Guangshe Li
page 357

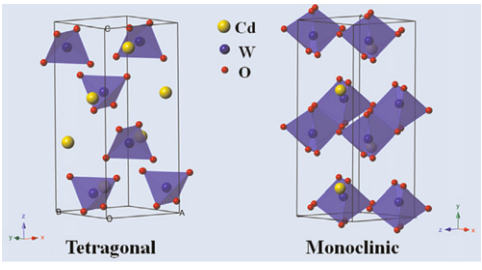

Monoclinic $CdWO_4$ exhibited a much higher photocatalytic activity than the tetragonal form owing to the lower symmetry, more distorted geometric structure, and the dispersive band configuration.

Mixed conductivity, structural and microstructural characterization of titania-doped yttria tetragonal zirconia polycrystalline/titania-doped yttria stabilized zirconia composite anode matrices
M.T. Colomer and M. Maczka
page 365

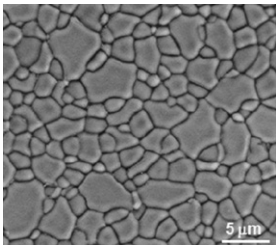

FE-SEM micrograph of a polished and thermal etched surface of a Ti-doped YTZP/Ti-doped YSZ composite material.

Syntheses, structures and luminescent properties of a series of 3D lanthanide coordination polymers with tripodal semirigid ligand
Junsheng Qin, Dongying Du, Lei Chen, Xiuyun Sun, Yaqian Lan and Zhongmin Su
page 373

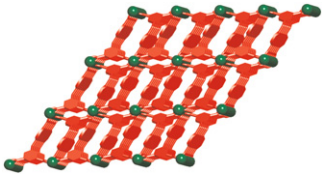

Reactions of the tripodal bridging ligand (H_3cpia) with lanthanide ions lead to the formation of a series of coordination polymers in the presence of formic acid or diethylamine.

Dicarboxylate assisted synthesis of the monoclinic heterometallic tetrathiocyanato bridged copper(II) and mercury(II) coordination polymer $\{Cu[Hg(SCN)_4]\}_n$: Synthesis, structural, vibration, luminescence, EPR studies and DFT calculations
Ali Akbar Khandar, Axel Klein, Akbar Bakhtiari, Ali Reza Mahjoub and Roland W.H. Pohl
page 379

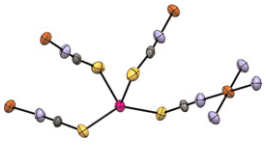

Synthesis and X-ray structure determination of the monoclinic $\{Cu[Hg(SCN)_4]\}_n$ is reported. The IR, far-IR, Raman, photoluminescence as well as EPR spectra of the compound is discussed. Also, the emission and semiconducting behavior of the compound is illustrated through the density functional theory calculation of electronic band structure along with density of states.

Improve the catalytic activity of α-Fe_2O_3 particles in decomposition of ammonium perchlorate by coating amorphous carbon on their surface
Yifu Zhang, Xinghai Liu, Jiaorong Nie, Lei Yu, Yalan Zhong and Chi Huang
page 387

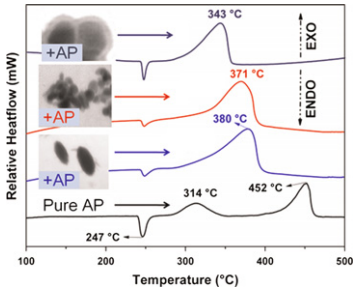

The catalytic performance of pod-like α-Fe_2O_3, sphere-like α-Fe_2O_3 and α-Fe_2O_3@C on the thermal decomposition of ammonium perchlorate (AP).

Room temperature ferromagnetism in undoped and Fe doped ZnO nanorods: Microwave-assisted synthesis
Mukta V. Limaye, Shashi B. Singh, Raja Das, Pankaj Poddar and Sulabha K. Kulkarni
page 391

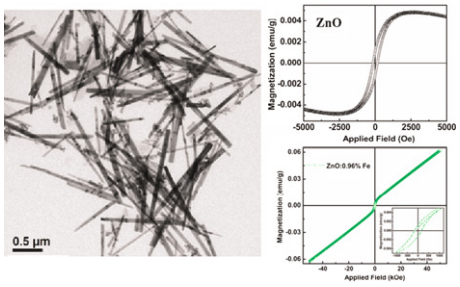

Room temperature ferromagnetism has been reported in undoped and Fe doped ZnO nanorods of average length ~1 μm and diameter ~50 nm.

Hydrothermal syntheses and structures of the uranyl tellurates $AgUO_2(HTeO_5)$ and $Pb_2UO_2(TeO_6)$
Jie Ling, Matthew Ward and Peter C. Burns
page 401

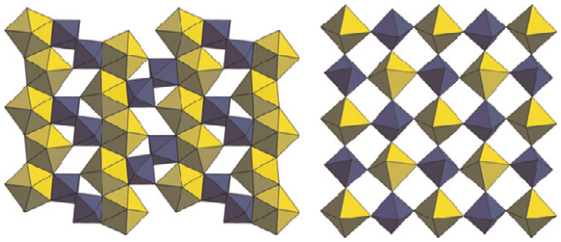

Two hydrothermally synthesized uranyl tellurates, $AgUO_2(HTeO_5)$ and $Pb_2UO_2(TeO_6)$, contain sheets built from uranyl pentagonal or square bipyramids, as well as tellurate octahedra.

Fluorine sites in glasses and transparent glass-ceramics of the system $Na_2O/K_2O/Al_2O_3/SiO_2/BaF_2$
Christian Bocker, Francisco Muñoz, Alicia Durán and Christian Rüssel
page 405

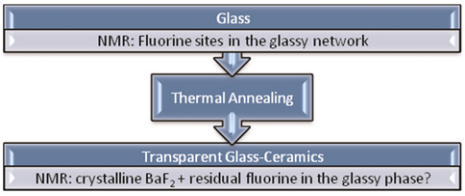

The X-ray diffraction and the nuclear magnetic resonance spectroscopy were applied to glasses in the silicate system $Na_2O/K_2O/SiO_2/BaF_2$ and the respective glass-ceramics with BaF_2 nano crystals in order to clarify the crystallization mechanism and the role of fluorine during crystallization.

Preferential growth orientation of laser-patterned $LiNbO_3$ crystals in lithium niobium silicate glass
T. Komatsu, K. Koshiba and T. Honma
page 411

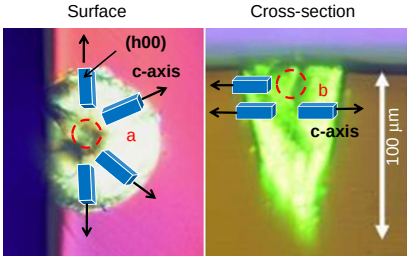

Polarized optical microscope observations for the surface and cross-section of the dot obtained by LD laser ($\lambda = 795$ nm) irradiations of $P = 1.4$ W and $t = 20$ s in Cu–LNS glass. Schematic model for the orientation of $LiNbO_3$ crystals at the edge parts of the surface and cross-section of the dot is also shown.

Assembly of two layered cobalt–molybdenum phosphates: Changing interlayer distances by tuning the lengths of amine ligands
Yu-Nan Zhang, Bai-Bin Zhou, Jing-Quan Sha, Zhan-Hua Su and Ji-Wen Cui
page 419

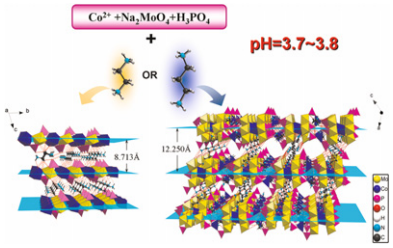

By using amines with different lengths, two layered cobalt–molybdenum phosphates with different interlayer distances have been hydrothermally synthesized.

Continued

***Ab initio* study of phase transition and bulk modulus of NaH**
Xiao-Wei Sun, Qi-Feng Chen, Xiang-Rong Chen, Ling-Cang Cai and Fu-Qian Jing
page 427

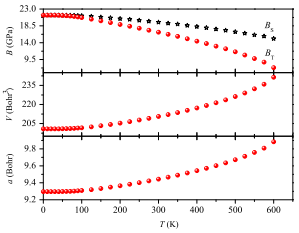

The isothermal bulk modulus B_T, adiabatic bulk modulus B_S, primitive cell volume V, and lattice constant a of an NaH with an NaCl-type structure as a function temperature T at zero pressure. When $T<100$ K, B nearly keeps constant; when $T>100$ K, B decreases dramatically as T increases. Correspondingly, when $T<100$ K, the primitive cell volume and lattice parameter of an NaH with an NaCl-type structure have a little change; when $T>100$ K, the primitive cell volume and lattice parameter changes rapidly as T increases. It is the rapid volume or lattice parameter variation that makes the bulk modulus B rapidly decrease.

Syntheses, and crystal and electronic structures of the new Zintl phases Na_2ACdSb_2 and K_2ACdSb_2 (A = Ca, Sr, Ba, Eu, Yb): Structural relationship with Yb_2CdSb_2 and the solid solutions $Sr_{2-x}A_xCdSb_2$, $Ba_{2-x}A_xCdSb_2$ and $Eu_{2-x}Yb_xCdSb_2$
Bayrammurad Saparov, Maia Saito and Svilen Bobev
page 432

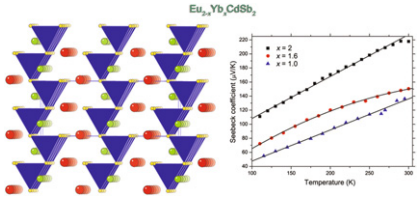

The quaternary Zintl phases Na_2ACdSb_2 and K_2ACdSb_2 (A = Ca, Sr, Ba, Eu, Yb) with novel layered structures have been synthesized for the first time and structurally characterized by single-crystal X-ray diffraction. Reported as well are the results from crystallographic and property studies of the closely related solid solutions $Sr_{2-x}A_xCdSb_2$, $Ba_{2-x}A_xCdSb_2$ ($x\approx1$), and $Eu_{2-x}Yb_xCdSb_2$ ($1<x\leq2$).

Thermal, optical and spectroscopic characterizations of borate laser crystals
M. Chavoutier, V. Jubera, P. Veber, M. Velazquez, O. Viraphong, J. Hejtmanek, R. Decourt, J. Debray, B. Menaert, P. Segonds, F. Adamietz, V. Rodriguez, I. Manek-Hönninger, A. Fargues, D. Descamps and A. Garcia
page 441

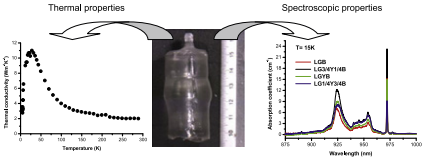

Several solid solutions of a rare earth borate were studied. The figure illustrates one of these single crystals obtained by Czochralski and shows thermal behaviour and absorption spectra at low temperature.

Structure and vibrational modes of AgI-doped AsSe glasses: Raman scattering and ab initio calculations
O. Kostadinova, A. Chrissanthopoulos, T. Petkova, P. Petkov and S.N. Yannopoulos
page 447

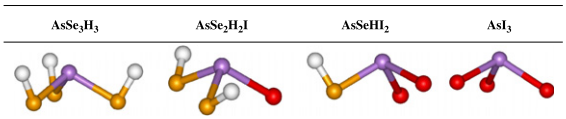

Raman scattering and *ab initio* calculations are employed to study the structure of AgI–AsSe superionic glasses. The role of mixed chalcohalide pyramidal units as illustrated in the figure is elucidated.

Novel pseudo-morphotactic synthesis and characterization of tungsten nitride nanoplates
Deliang Chen, Hejing Wen, Tao Li, Li Yin, Bingbing Fan, Hailong Wang, Rui Zhang, Xinjian Li, Hongliang Xu, Hongxia Lu, Daoyuan Yang, Jing Sun and Lian Gao
page 455

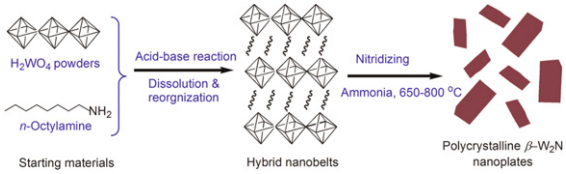

A novel pseudo-morphotactic transformation route was developed to synthesize β-W_2N nanoplates by thermally treating tungstate-based inorganic–organic hybrid nanobelts, the morphology of which was inherited to the β-W_2N nanocrystals.

Structural and magnetic properties of $RMn_{2-x}Fe_xD_6$ compounds (R = Y, Er; $x\leq0.2$) synthesized under high deuterium pressure
V. Paul-Boncour, S.M. Filipek, R. Sato, R. Wierzbicki, G. André, F. Porcher, M. Reissner and G. Wiesinger
page 463

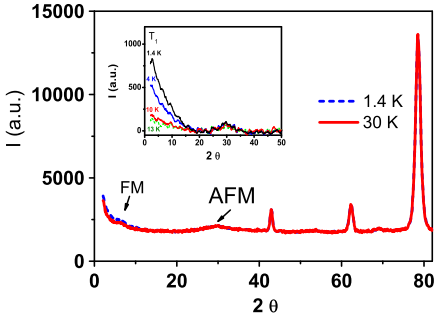

Neutron powder diffraction (NPD) patterns of $ErMn_{1.8}Fe_{0.2}D_6$ at 1.4 and 30 K measured on G4.1 spectrometer. *Inset*: difference curves between the NPD patterns measured at T_1 and 30 K showing ferromagnetic (FM) and antiferromagnetic (AFM) short range order.

A comparison of the transport properties of lithium-stuffed garnets and the conventional phases $Li_3Ln_3Te_2O_{12}$
Edmund J. Cussen, Thomas W.S. Yip, Gemma O'Neill and Michael P. O'Callaghan
page 470

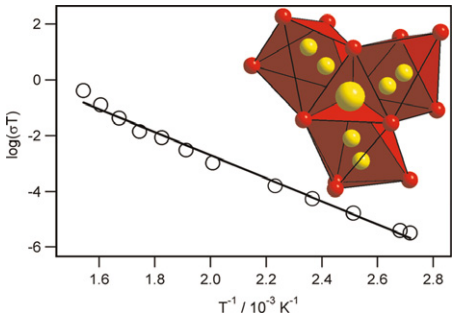

The lithium-stuffed garnets $Li_6CaLa_2Sb_2O_{12}$ and $Li_{6.4}Ca_{1.4}La_{1.6}Sb_2O_{12}$ accommodate lithium in a complex distribution across oxide tetrahedra and octahedra. The total conductivity of $Li_6CaLa_2Sb_2O_{12}$ is considerably lower than reported for related fast-ion conducting garnets due to a much larger intra-grain contribution to the resistivity than is commonly found for this family of compounds.